# Vortex configurations in thin superconducting equilateral triangles

L. R. E. Cabral* and J. Albino Aguiar
*Departamento de Física, Universidade Federal de Pernambuco, Recife 50670-901, PE, Brazil*
(Received 2 September 2009; revised manuscript received 3 November 2009; published 28 December 2009)

We investigated theoretically vortex configurations in thin mesoscopic superconducting equilateral triangles submitted to an external magnetic field. Analytical expressions for the vortex interactions with the screening current and other vortices were calculated by considering the sample sides much smaller than the effective penetration depth within the London limit. The vortex configurations were obtained by using Langevin dynamics simulations. In most of the configurations, the vortices sit close to the corners, presenting twofold or threefold symmetry. We also determined the dependence on the magnetic field of the equilibrium states. The ground states with larger magnetic field range are those with the number of vortices equal to the triangular numbers [$N'=n(n+1)/2$, with $n$ integer]. A study of different stable configurations with the same number of vortices is also presented.

DOI: 10.1103/PhysRevB.80.214533 PACS number(s): 74.20.De, 74.25.Dw, 74.25.Ha

## I. INTRODUCTION

The study of the vortex matter in mesoscopic superconductors has been subject of great interest, particularly, because of the resemblance with the atomic matter. This is a result of the interplay between vortex-vortex repulsion and the confinement produced by the external magnetic field-induced screening currents (see, for instance, Refs. 1–5). In circular geometries (thin disks and superconducting cylinders), for low number of vortices (low total vorticity), vortex configurations are arranged in shells and have magic numbers[1,3–6] (similar to electronic states in atoms). For higher number of vortices, an Abrikosov (hexagonal) vortex arrangement appears in the center of the disk surrounded by two or more vortex shells.[4] In superconducting slabs,[7–9] squares,[10–12] rectangles,[11,13,14] ellipses[15] (there is also a connection of these systems and two-dimensional clusters of classical charged particles trapped in an anisotropic parabolic potential[16]), and triangles[11,17] (although in this particular case large mesoscopic samples have not been studied), vortex systems have also been theoretically studied by using either the Ginzburg-Landau (GL) or the London approaches. In these cases, similarly to the circular geometry, vortex configurations obey the superconductor geometry for low total vorticity; while, for large systems and higher vorticity, a hexagonal arrangement appears close to the center of the superconductor. Moreover, due to the adjustment of a hexagonal lattice into a confined geometry, vortex with a coordination number different from six appears close to the sample edges, in the form of topological defects in the lattice (such as disclinations and dislocations).[4]

In superconductors, the vortex matter has been successfully described by the GL theory.[18–20] This phenomenological theory attributes to the superconducting regions a complex order parameter $\Psi=|\Psi|e^{i\theta}$ (where $|\Psi|^2$ is proportional to the superconducting electrons density). It also considers the current density $\boldsymbol{j}$ and the vector potential $\boldsymbol{A}$ related by $\lambda^2\boldsymbol{j}\sim|\Psi|^2(\nabla\theta-\boldsymbol{A})$, where $\lambda$ is the London penetration depth. The time-dependent version of this theory has also succeeded in describing nonequilibrium vortex phenomena, although its range of applicability is more restricted than the time-independent GL theory.

The London approach can be derived from the GL theory by considering the order-parameter absolute value $|\Psi|$ uniform throughout the entire superconductor. Nonetheless, it can be shown from the BCS microscopic theory that this approach is valid for the whole temperature range $0\leq T\leq T_c$ as long as $\lambda(T)\gg(1/\xi+1/l)^{-1}$, where $l$ is the mean free path, and the superconducting electron density $n_s(\mathbf{r})$ is approximately uniform.[21] Equivalently, this means making $\xi\rightarrow 0$. The presence of vortices is accounted by taking singularities in the order-parameter phase $\theta$, which results from treating a zero size vortex core (of radius $\sim\xi$). This approach works well if the inter vortex distance $a_v$ is reasonably larger than the actual value of $\xi$, i.e., in the case of nonoverlapping vortex cores. Therefore, by calculating the vortex interactions with the screening currents and with other vortices, one can obtain the vortex dynamics, as well as vortex stable states.

Recently, vortex configurations have also been studied in superconducting triangles, by using either the Ginzburg-Landau theory[22,23] or the London approach.[24] The former studies apply to small-sized superconductors (sizes of the order of $\xi$), while the latter can be applied to relatively large systems (size of several $\lambda$). Although applicable to the London limit, the present study is intended to the case $\xi\ll a\ll\Lambda=\lambda^2/d$, where $a$ and $d$ are the length of the triangle sides and the triangle thickness, respectively. This yields vortex-vortex interactions, as well as the vortex interactions with the boundaries and the shielding currents, quite different than the ones studied, for example, in Ref. 24, which are short ranged. Here, vortex-vortex interactions are long ranged.

This paper is organized as follows. Section II presents the theoretical formalism, which was used in order to find the screening currents and the forces acting on each vortex. The numerical approach is detailed in Sec. III. The discussion of the results is presented in Sec. IV. This section is divided in two parts. In the first part, we discuss the vortex ground states. The second part—dealing with metastable vortex states—is further split in two parts. The first considers configurations containing only singly quantized vortices (SQVs), carrying only one flux quantum $\Phi_0$. In the second part, we investigate the possibility of configurations with multiply

 

quantized vortices (MQVs). Finally, we present our conclusions in Sec. V.

## II. THEORETICAL FORMALISM

We considered a system with $N$ vortices inside a superconducting equilateral triangle of side $a$. The applied magnetic field $\boldsymbol{H}=H_a\hat{z}$ is applied along the triangle thickness $d$, where $d \ll a \ll \Lambda=\lambda^2/d$ ($\Lambda$ is the effective penetration depth and $\hat{z}$ is a unit vector perpendicular to the film). Within this limit and by using the London approach, the triangle consists of a two-dimensional system with pointlike vortex cores. The vortex-vortex interactions are logarithmic since $|\boldsymbol{r}_i-\boldsymbol{r}_j| \leq a \ll \Lambda$ (where $\boldsymbol{r}_i$ is the position of the $i^{\text{th}}$ vortex core). These pairwise forces can be computed from the Lorentz force acting on a vortex core $\boldsymbol{f}_L=\Phi_0\boldsymbol{J}\times\hat{z}$, where $\Phi=h/2e=2.07\times10^{-15}$ Wb.

The time-independent Ginzburg-Landau theory for isotropic superconductors describes phenomenologically the superconducting state by the Gibbs free-energy functional,

$$\mathcal{G}=\mathcal{G}_n+\mu_0 H_c^2\int_V d^3r\left[-|\Psi|^2+\frac{1}{2}|\Psi|^4+|(\nabla-i\boldsymbol{A})\Psi|^2+\kappa^2|\boldsymbol{H}-\boldsymbol{H}_a|^2\right]. \tag{1}$$

Here, $\mathcal{G}_n$ is the normal-state free energy, $H_c$ is the thermodynamical critical magnetic field, $V$ is volume occupied by the superconductor, $\boldsymbol{A}$ is the vector potential, $\boldsymbol{H}$ is the local magnetic field, $\kappa=\lambda/\xi$ is the Ginzburg-Landau order parameter, and $\Psi=|\Psi|\exp(i\theta)$ is the complex order parameter. In this equation, it should be noticed that lengths are in units of the coherence length, $\xi$, $\boldsymbol{A}$ in units of $\Phi_0/2\pi\xi$, $\boldsymbol{H}$ in units of $H_{c2}$, and $\Psi$ is in units of $\Psi_o$ (which is the value faraway from the interfaces). It is useful to rewrite Eq. (1) (in fact the Ginzburg-Landau energy density) in a slightly different form,

$$\mathcal{G}=\mathcal{G}_n+\mathcal{G}_{\text{core}}+\mathcal{G}_{\text{kin}}, \tag{2a}$$

where

$$\mathcal{G}_{\text{core}}=\frac{\mu_0 H_c^2}{V}\int_V d^3r\left[-|\Psi|^2\left(1-\frac{1}{2}|\Psi|^2\right)+(\nabla|\Psi|)^2\right] \tag{2b}$$

and

$$\mathcal{G}_{\text{kin}}=\frac{\mu_0 H_c^2}{V}\int_V d^3r(|\Psi|^2Q^2+\kappa^2|\boldsymbol{H}-\boldsymbol{H}_a|^2) \tag{2c}$$

are the core and kinetic-energy densities, respectively. The kinetic momenta of the Cooper pairs are proportional to the superconducting velocity $\boldsymbol{Q}=\nabla\theta-\boldsymbol{A}$. When minimizing the Ginzburg-Landau free energy [Eq. (1)] with respect to the order parameter and the vector potential, the Ginzburg-Landau equations,

$$(-i\nabla-\boldsymbol{A})^2\Psi=\Psi(1-|\Psi|^2), \tag{3a}$$

$$\kappa^2\boldsymbol{j}=\kappa^2\nabla\times\nabla\times\boldsymbol{A}=|\Psi|^2\boldsymbol{Q}, \tag{3b}$$

are obtained. Here, the current density is in units of $H_{c2}/\xi$. The boundary conditions, which must be satisfied along a superconductor/vacuum interface $\partial V$, are

$$\hat{n}\cdot(-i\nabla-\boldsymbol{A})\Psi|_{\partial V}=0, \tag{4a}$$

$$\hat{n}\cdot\boldsymbol{j}|_{\partial V}=0, \tag{4b}$$

where $\hat{n}$ represents the outward unit vector to the interface.

The so-called London limit can be derived from either the microscopic or the Ginzburg-Landau theories by taking the limit $\xi\to0$, if there is no appreciable vortex cores overlapping. This means that the modulus of the complex order parameter $|\Psi(\boldsymbol{r})|$ can be considered uniform over the whole sample (except at the vortex core, where it should be zero). However, the phase of the order parameter should vary by $2\pi n(n=0,\pm1,\pm2,\pm3,\ldots)$ for every closed path, which includes a vortex core inside. Therefore, the vortex currents, as well as the external magnetic field screening current, can be calculated from the London equation,

$$\kappa^2\boldsymbol{j}+\boldsymbol{A}=\nabla\theta=\sum_{i=1}^{N}\hat{z}\times\frac{\boldsymbol{r}-\boldsymbol{r}_i}{|\boldsymbol{r}-\boldsymbol{r}_i|^2}, \tag{5}$$

which is the second Ginzburg-Landau equation [Eq. (3b)], with $|\Psi|=1$ everywhere. Here, the function in the right-hand side accounts for the presence of vortex cores at $\boldsymbol{r}_i=(x_i,y_i)$, arising from the singularities of the order-parameter phase $\theta$.[1,21] It is worth to notice that although the London limit considers a vanishing vortex core size, a fairly good approximation for the behavior of the order parameter close to the vortex core[19,25] removes the divergence of the right-hand side in Eq. (5) by replacing $|\boldsymbol{r}-\boldsymbol{r}_i|$ with $\sqrt{|\boldsymbol{r}-\boldsymbol{r}_i|^2+2\xi^2}$.

In the limit $\Lambda \gg a \gg d$, the local magnetic field can be approximated by the external magnetic field, i.e., $\boldsymbol{H}\approx H_a\hat{z}$. Therefore, after averaging along the film thickness, Eq. (5) becomes

$$-\hat{z}\frac{\kappa^2}{d}\nabla^2 g+\hat{z}H_a=\hat{z}2\pi\sum_{i=1}^{N}\delta(\boldsymbol{r}-\boldsymbol{r}_i), \tag{6}$$

where the sheet current density $\boldsymbol{J}(x,y)=\int_0^d dz\boldsymbol{j}(x,y,z)\approx d\boldsymbol{j}(x,y,d/2)$ and the streamline function $g(x,y)$ (which can be regarded as a local magnetization along $z$ in the thin film[26]) are related by $\boldsymbol{J}=\nabla\times(\hat{z}g)=-\hat{z}\times\nabla g$. Interestingly, as pointed out by Fetter,[27] the streamline function and the phase of the order parameter are related to the real and imaginary parts of a complex-valued function, $\Omega(z,z_j)=i[\theta(z,z_j)+iG(z,z_j)]=-G(z,z_j)+i\theta(z,z_j)$, where $z=x+iy$ and $G(z,z_j)=(\kappa^2/d)g(z,z_j)$ (see also Refs. 4 and 28). This can be verified, in the absence of external magnetic field, by writing Eq. (5) in complex notation,

$$i\overline{\frac{d\Omega}{dz}} = \frac{\partial G}{\partial y} - i\frac{\partial G}{\partial x} = \left(\frac{\partial \theta}{\partial x} + i\frac{\partial \theta}{\partial y}\right)$$
$$= i\left[\frac{\partial(-G)}{\partial x} - i\frac{\partial \theta}{\partial x}\right]$$
$$= i\sum_{j=1}^{N} \overline{\frac{z-z_j}{|z-z_j|^2}}$$
$$= i\sum_{j=1}^{N} \overline{\frac{d}{dz}\ln(z-z_j)}, \tag{7}$$

where the bar means complex conjugation. This equation yields $\Omega(z,z_j)=\Sigma_{j=1}^{N}\ln(z-z_j)$. This corroborates that both $g$ and $\theta$ satisfy Laplace equation (except at the vortex cores), as stated by Eq. (6) for $H_a=0$.

For a superconducting medium surrounded by vacuum (which is equivalent to a confined system of vortices), the boundary conditions [Eqs. (4a) and (4b)] are satisfied for $g(\boldsymbol{r})|_{\partial V}$=const along the interface. For the case of a simply connected superconductor, that is, with no holes inside the sample, it is enough to consider $g(\boldsymbol{r})|_{\partial V}=0$ (for multiply connected superconductors, see Refs. 29 and 30).

The solution of Eq. (5) can be written as $g=g_H+g_v$, where $g_H$ and $g_v$ are the response to the external magnetic field and to the presence of vortices, respectively. $g_H$, which is the solution of $\nabla^2 g_H=(d/\kappa^2)H_a$, is given by

$$g_H(\boldsymbol{r}) = \frac{H_a d}{4\kappa^2}\left(1-\frac{y}{h_\Delta}\right)\left[\left(\frac{\sqrt{3}x}{a}\right)^2 - \left(\frac{y}{a}\right)^2\right], \tag{8}$$

where $h_\Delta=\sqrt{3}a/2$ is the triangle height and $g$ is given in units of $H_{c2}\xi$.

The streamline function due to the vortices for $N$ vortices in an infinite thin film is given by $g_v(\boldsymbol{r},\boldsymbol{r}_i)=(d/\kappa^2)\Sigma_{i=1}^{N}\ln(|\boldsymbol{r}-\boldsymbol{r}_i|)$. For an equilateral triangle, the zero net current flow across the interface is satisfied by adding vortex images outside the triangular domain. For a vortex core at $(x_i,y_i)$, this results in an infinite set of rectangular domains, each one with sides $3a$ and $\sqrt{3}a$, and containing 6 vortices (antivortices) placed at $(x_I,y_I)[(x_I,-y_I)]$,

$$I=1 \rightarrow (x_i,y_i),$$

$$I=2 \rightarrow [-0.5(x_+-3a), h_\Delta-0.5y_-],$$

$$I=3 \rightarrow (-0.5x_+,-0.5y_-),$$

$$I=4 \rightarrow [0.5(x_--3a), h_\Delta-0.5y_+],$$

$$I=5 \rightarrow (0.5x_-,-0.5y_+),$$

$$I=6 \rightarrow [x_i-3a\ \mathrm{sign}(x_i)/2, y_i-h_\Delta]. \tag{9}$$

Here $x_\pm=\pm x_i+\sqrt{3}y_i$ and $y_\pm=\pm\sqrt{3}x_i+y_i$. Therefore,

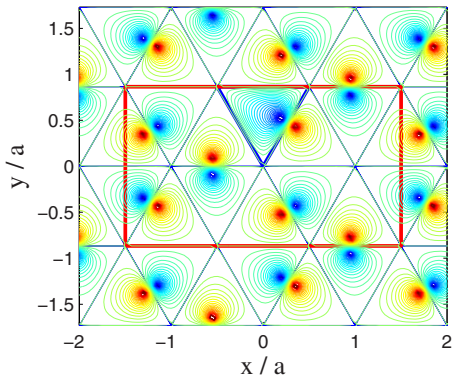


FIG. 1. (Color online) Current streamlines (contour lines of $g_v$) for a vortex at $(0.35a,0.5h_\Delta)$ and its images. In the triangle defined by the points (0, 0), $(0.5a,h_\Delta)$, and $(-0.5a,h_\Delta)$ (corresponding to the superconducting domain), the contour lines of $g_H$ for $H_a=0.001$ are also plotted. A rectangle is drawn to help visualize the vortex images periodic structure given in Eq. (9).

$$g_v(\boldsymbol{r},\boldsymbol{r}_i) = \frac{1}{2}\sum_{m=-\infty}^{\infty}\sum_{n=-\infty}^{\infty}\sum_{I=1}^{6} \times \ln\left[\frac{(x-x_I-3ma)^2+(y-y_I-\sqrt{3}na)^2}{(x-x_I-3ma)^2+(y+y_I-\sqrt{3}na)^2}\right], \tag{10}$$

where the index $I$ refers to the positions of the vortices and antivortices as defined in Eq. (9). Figure 1 shows the current streamlines for a vortex core placed at $(0.35a,0.5h_\Delta)$, as well as its images. The vortex images periodic unit cell is enclosed by a rectangle. Also, the superconducting triangle—defined by the points (0, 0), $(0.5a,h_\Delta)$, and $(-0.5a,h_\Delta)$—depicts the current streamlines of $g_H$ for $H_a=0.001$.

The forces acting on the vortices derived from the Lorentz force are proportional to the gradient of the streamline functions. The force acting on the $i$th vortex can be written as $\boldsymbol{f}_i=\boldsymbol{f}_i^a+\Sigma_j\boldsymbol{f}_{i,j}$, where $\boldsymbol{f}_i^a \propto -\nabla g_H(\boldsymbol{r})|_{\boldsymbol{r}_i}$ (interaction with screening currents) and $\boldsymbol{f}_{i,j}\propto -\nabla_j g_v(\boldsymbol{r}_i,\boldsymbol{r}_j)$ (interaction with other vortices). When considering the term $i=j$, it is important to take into account the interaction of the $i$th vortex with its own images (outside the triangular domain).

The shielding sheet current density $\boldsymbol{J}_H=-\hat{z}\times\nabla g_H$ has components (in units of $H_{c2}$)

$$J_{H,x}(\boldsymbol{r}) = \frac{H_a d}{2\kappa^2}\left\{\frac{y}{a}+\frac{3a}{2h_\Delta}\left[\left(\frac{x}{a}\right)^2-\left(\frac{y}{a}\right)^2\right]\right\}, \tag{11a}$$

$$J_{H,y}(\boldsymbol{r}) = \frac{3H_a d}{2\kappa^2}\left(1-\frac{y}{h_\Delta}\right)\frac{x}{a}. \tag{11b}$$

One may observe that the vector potential of the applied magnetic field $\boldsymbol{H}_a$ is obtained by using the London equation in the absence of vortices $\boldsymbol{A}_a=-\kappa^2\boldsymbol{j}_H=-\kappa^2\boldsymbol{J}_H/d$. Since this divergent free vector potential has zero components normal to the triangle edges, it can be used as a gauge for solving the Ginzburg-Landau equations.[31–33]

### III. NUMERICAL APPROACH

We employed a Langevin dynamics algorithm to simulate the vortex dynamics. The forces calculated in Sec. II, $\boldsymbol{f}_i^a$ and $\boldsymbol{f}_{i,j}$, were used in the Bardeen-Stephen equation of motion,[34]

$$\eta\frac{d\boldsymbol{r}_i}{dt} = \boldsymbol{f}_i^a + \sum_j \boldsymbol{f}_{i,j} + \boldsymbol{\Gamma}_i, \tag{12}$$

where the term $j=i$ is included in the summation in order to account for the vortex interaction with its images and a stochastic random force is added, which takes into account thermal fluctuations. This stochastic force has a random white-noise spectrum and obeys the fluctuation-dissipation theorem,

$$\langle \Gamma_{\alpha,i}(t)\Gamma_{\beta,j}(t')\rangle = 2\eta\delta_{\alpha\beta}\delta_{ij}\delta(t-t')k_BT, \tag{13}$$

where $\langle\ \rangle$ means average value, $k_B$ is the Boltzmann's constant, $T$ is the temperature, $\eta \approx d\mu_0\Phi_0 H_{c2}/\rho_n$ is the viscous drag coefficient ($\rho_n$ is the resistivity in the normal state), and Greek and italic indexes refer to vector components and vortex labels, respectively. We applied the leap-frog scheme for the time integration scheme, as described in Ref. 35. The time step used varied according to $\Delta t = \Delta t_1 + \Delta t_0/(1+\mathcal{V}^4)$, where $\Delta t_1 = 10^{-5}$, $\Delta t_0 = 5\times 10^{-4}$, and $\mathcal{V}$ is a term proportional to the maximal velocity of the vortices at that time step. The nonconstant time step allows for achieving higher accuracy when vortex displacements are large, while speeding up computation time for smaller vortex displacements.

One difficulty that may arise in implementing numerically Eq. (10) for the vortex-vortex forces comes from the infinite number of terms in the summations. Usually, one should not truncate infinite series of logarithmic interactions since this kind of potential is slow decaying,[36] contrary to interactions, which present exponential decay.[37] In our case, this is not so problematic because we are dealing with vortices and antivortices, which, at long distances, may act as vortex dipoles, generating a $1/r$-like potential. Nevertheless, we preferred to employ a technique, which allows for a rapid converging series summation,[36] therefore, avoiding the truncation of the series and implementing the *full summation* of the *contributions* of *both vortices and antivortices images*.

In order to obtain different metastable configurations with a given total vorticity for a magnetic field $H_a$, we first distribute the vortices randomly inside the triangular domain. Then, we let the system evolve in time according to Eq. (12). A metastable configuration is found when the maximal vortex velocity was smaller than $\sim 2\times 10^{-10}$ (in units of $\xi$). When this criterion is achieved, a new attempt is performed with a new random vortex distribution and subsequent integration of Eq. (12). We typically performed 1000 attempts for given values of the total vorticity $L$, number of vortices $N$, and applied magnetic field $H_a$ in order to have a reasonable collection of possible vortex configurations. We considered low total vorticity states, ranging from $L=0$ to $L=37$, with $H \leq 0.05H_{c2}$ (however, we used $H \leq 0.03$ for configurations with $L<21$ in order to save computational time).

The equilibrium vortex state at a given applied field was obtained by calculating the energy from Eq. (1) of all the different vortex configurations at $H_a$. Strictly speaking, the procedure described above does not ensure that the configuration is actually the equilibrium state since it is possible that some configuration with lower energy was not generated. However, the probability that it is so is much greater than otherwise, due to the number of attempts performed (at least for low number of vortices). The order parameter was calculated approximately by the following procedure: the phase of the order parameter $\theta$ was computed from a given stable vortex configuration by using Eq. (10) (this was also used to solve numerically the Ginzburg-Landau equations in disk, rings, and squares by using the analytical expressions for the phase of the order parameter in Ref. 28); with the analytical values for $\theta$ and the vector potential for the applied magnetic field $\boldsymbol{A}_a$, the real part of the first Ginzburg-Landau equation (3a) was solved numerically by using the relaxation method. We chose a regular uniform equilateral triangular grid of size about $0.26\xi$ (the sample side was discretized by 384 points). In fact, this procedure is very similar to including holes in the sample at the vortex core positions filled with $p_i$ fluxoid quanta each. This allowed us to obtain the modulus of the order parameter $|\Psi|$ and, therefore, calculate approximately the Ginzburg-Landau free energy of a given vortex configuration.

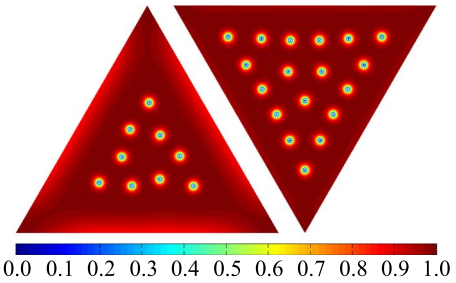


FIG. 2. (Color online) Modulus of the order parameter ($|\Psi|$) for metastable configurations with $L=9$ at $H=0.0210$ (left) and with $L=18$ at $H=0.0220$ (right). The color map varies from blue ($|\Psi| \approx 0$) to red ($|\Psi| \approx 1$).

When considering multiply (giant) quantized vortices in the vortex configurations, the procedure was basically the same as above but taking the vorticity of the giant vortex $i$ as $p_i > 1$. This implies that the phase of the order parameter, the corresponding streamline function, and the forces acting on vortices are multiplied by $p_i$. In this manner, we were able to successfully include MQV in our simulations.

The error associated with our calculation of the Ginzburg-Landau energy is estimated to be $\sim 10^{-4}\mu_0 H_c^2/2$. It is in part related to the truncation the vortex cores position onto the uniform grid used. The estimation was performed by computing the energy of vortex configurations at magnetic fields close to or above $H_{c2}$. For example, for the sample dimensions considered, the energy of the configuration with one SQV differs from zero by a quantity about $4\times 10^{-5}$ (in units of $\mu_0 H_c^2/2$).

In Fig. 2, the modulus of the order parameter ($|\Psi|$) calculated from the above procedure is depicted for two stable configurations with $L=9$ (at $H=0.0210$) and with $L=18$ (at $H=0.0220$). As one can observe, it is in very good agreement with $|\Psi|$ computed by other approaches.[11,23,38]

We finally studied the magnetic field dependence of several vortex configurations (usually the most stable ones ob-

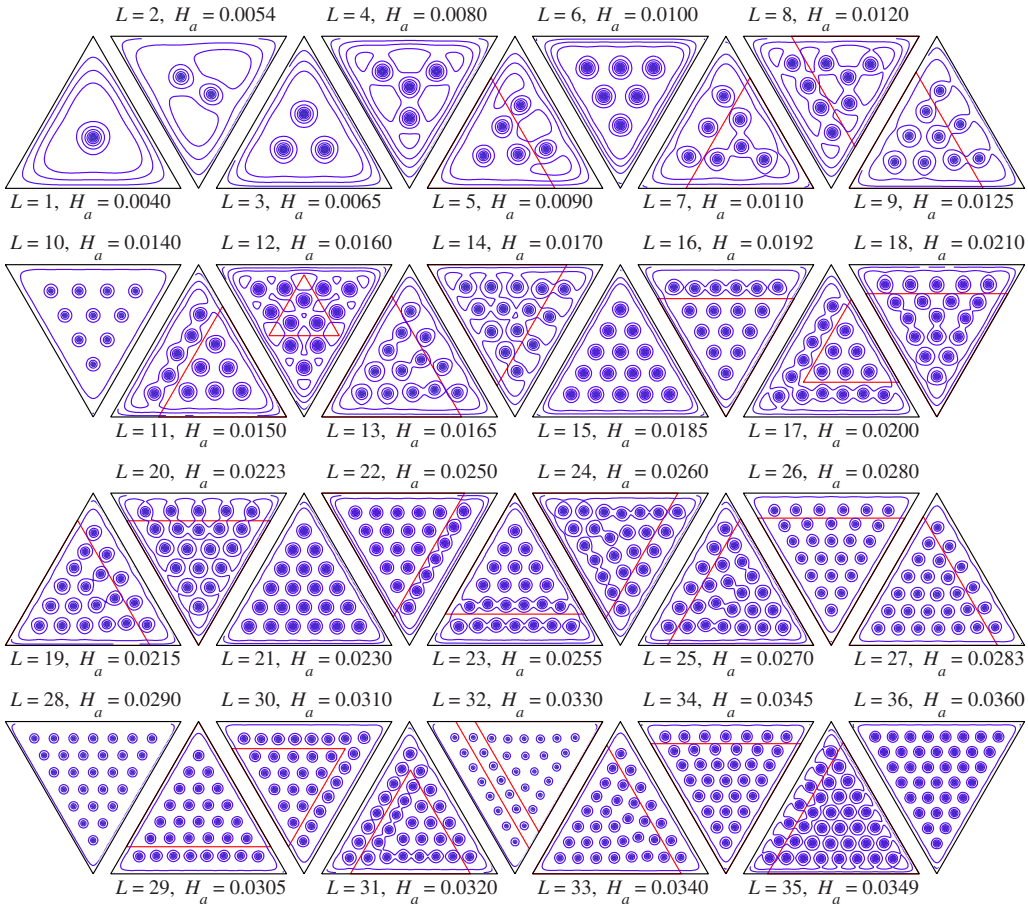


FIG. 3. (Color online) Current streamlines of the ground-states vortex configurations from $L=1$ to $L=36$. Notice that each figure depicts a different configuration observed at different conditions. The total vorticity and the magnetic field at which the configuration was obtained are shown at the top or the bottom of each figure. Each vortex configuration can be viewed as being formed by vortex "bricks," i.e., lower vorticity configurations plus linear chain of vortices. The red straight lines are guides for the eyes to help visualize the smaller configurations "bricks," which form a configuration of higher $L$. The nomenclature for each configuration is explained in the body of text and is also shown in Table I.

tained from the previous procedure). This was achieved in the following way. For a given ground-state configuration, the magnetic field $H_a$ was set at a high-field value (where it is expected to be well above the range in which the stable configuration is the ground state). Then $H_a$ was swept down by field steps $\Delta H_a=2.0\times10^{-5}$. The magnetic field was changed after a time interval $2\times10^6\Delta t_1$. This process was done until reaching $H_a=0$, which allowed to observe the vortex states transitions. Therefore, we could investigate the magnetic field range of the equilibrium states (by calculating approximately the Ginzburg-Landau energy). We also obtained the critical magnetic fields ($H_{\mathrm{unst}}$) below which each configuration ceases to be stable (only within the London limit). Therefore, due to the limitations of our theoretical framework and numerical procedure, our results are restricted to magnetic fields much smaller than $H_{c2}$.

## IV. RESULTS

### A. Ground states

After performing the numerical procedure discussed in the previous section, we obtained the stable vortex configurations with number of vortices up to $N=37$ for given values of the magnetic field. The resulting configurations considered also multiply quantized (giant) vortices (MQV) (cf. Sec. IV B 2), but it turned out that the ground states are constituted by only SQV ($L=N$ for these configurations). Besides, for each $N$ value, several different configurations can be found. We call the one with lowest energy the ground state (for those values of $L$ and $H_a$).[39] In Fig. 3, the current streamlines of the ground-states configurations with $L=1$ to $L=36$ are plotted. The magnetic fields at which these configurations were obtained are also depicted in Fig. 3, at the top or at the bottom of each picture. It is observed that the competition between vortex-vortex repulsion and the compression on the vortex configuration due to the shielding currents generates vortices aligned with the edges and sit on the corners.[33] Moreover, as the number of vortices increases ($N>6$), there is a tendency for an Abrikosov-like vortex distribution, although defects on the vortex arrangements do appear if $N\neq10,15,21,28,36,\ldots$. The configurations depicted in Fig. 3 can also be useful for comparison with experimental data.

The configurations with $L$ equal to the triangular numbers, i.e., $N'=n(n+1)/2$, with $n$ integer, have the Abrikosov hexagonal lattice arrangement, with intervortex distance $a_v$ roughly uniform, which results from the vortex-vortex (radially symmetric) interaction. In addition, they present both threefold axial rotation and middle-plane reflexion symmetries, which satisfy the confinement (triangular) geometry. These configurations are very stable, presenting a range of stability broader than the other configurations. The other two configurations shown with both symmetries are the $L=4$ and $L=12$ (although without the Abrikosov lattice arrangement) ground-states configurations. Except from the configuration with $L=31$ (which do not possess any symmetry), the other configurations depicted (i.e., $L=2$, $L=5$, $L=7$, $L=8$, $L=9$, $L=11$, $L=13$, $L=14$, $L=16$, $L=17$, $L=18$, $L=19$, $L=20$, $L=22$, $L=23$ $L=24$, $L=25$, $L=26$, $L=27$, $L=29$, $L=30$, $L=32$, $L=33$, $L=34$, and $L=35$) have the middle-plane reflection symmetry. One of the reasons why the middle-plane reflection symmetry seems to be preferred apparently comes from the fact that frequently the vortex arrangements are less distorted and the intervortex distance is more uniform in this symmetry if compared to a configuration with only threefold axial rotation symmetry.

Interestingly, configurations with higher number of vortices can be viewed as being constructed by configurations with lower number of vortices. Therefore, red straight lines are drawn in Fig. 3 to help the visualization of these lower vorticity configurations. As an example, take the vortex ground state with 12 vortices. It seems to be made of a central $L=3$ surrounded by other three $L=3$ configurations. The $L=9$ vortex ground state seems to be constituted by a $L=6$ vortex ground states plus three vortices aligned along a line, while the $L=18$ vortex ground state looks like to be built from $L=9$ ground state, in addition to two linear vortex chains with four and five vortices each. Other examples like these can be found, which suggest a nomenclature for states with high number of vortices based on lower total vorticity states (which could be thought as fundamental bricks). Therefore, the $L=12$ ground state could be named $(4t3s1)$, where $4t$ would refer to the threefold symmetry with four $L=3$ ground states, where the $(3s1)$ represent this $L=3$ state constituted by three SQV. Another example is the configuration with $L=7$. It can be viewed as formed by the $L=4$ configuration plus a chain of three vortices $(r4s1+l3s1)$ $[(r4s1)$ referring to the $L=4$ ground state, where the $r$ means that the configuration has middle-plane reflexion symmetry, while $(l3s1)$ refers to a linear chain of three singly quantized vortices]. The $L=9$ would be $(t6s1+l3s1)$, the $L=13$ could be $(r9s1+l4s1)$, and the $L=18$ ground state would be $(r9s1+l4s1+l5s1)$ or $(r13s1+l5s1)$. In this manner, the higher $L$ vortex configurations can be viewed as being formed by lower $L$ configurations (the description of the other ground-state configurations using this nomenclature is given in Table I). Of course, this nomenclature cannot define all the configurations unambiguously but would be of great help in distinguishing between configurations with same number but with different arrangements of vortices. Nevertheless, all the configurations observed can be represented by smaller "bricks," i.e., a combination of configurations with $N'=n(n+1)/2$ ($n$ integer) vortices and linear vortex chains.

The dependence of the energy on the magnetic field was calculated for vortex states from $L=0$ to $L=37$. This allowed us to obtain the magnetic field range within which a given vortex configuration is the ground state. Figure 4 depicts the energy ($\Delta E_{\mathrm{GL}}=\mathcal{G}-\mathcal{G}_n$ in units of $\mu_0 H_c^2/2$) and the total vorticity $L$ as functions of the applied field $H_a$. Both the curves for the energy and the total vorticity stop at a certain magnetic field $H_{\mathrm{unst}}$. For $H_a<H_{\mathrm{unst}}$, the configuration with that value of $L$ ceases to be stable and a transition to another stable vortex state occurs. In this figure, three vortex states are stable at $H_a=0$: the (trivial) $L=0$, the $L=1$ vortex states, and the $L=2$ giant vortex state $(1g2)$, where the vortex is doubly quantized. The other configurations studied present $H_{\mathrm{unst}}\neq 0$.

In Fig. 4, the magnetic field range, where a given configuration is the ground state, is marked by a "staircase" thick line. $H_{\mathrm{unst}}$ as well as the initial $H_1$ and final $H_2$ magnetic fields of the region over which a vortex configuration with total vorticity $L$ is in the ground state (also the field range of this stability, $\Delta H_{\mathrm{stab}}=H_2-H_1$) are shown in Table I.

Our study shows that the ground states are characterized by SQV. For example, states with giant vortices—the $L=2$ state with one giant vortex [$(1g2)$-state] and the $L=5$ state composed of one giant and three singly quantized vortices [$(3s1,1g2)$-state]—are also shown in Fig. 4 by lines with circles.[40] They have a higher energy than the corresponding $L$ states with only singly quantized vortices. Other configurations, containing giant vortices, were also obtained (see next section), but none of them had lower energy than the ones composed of singly quantized vortices.

The dependence of the magnetization on the external magnetic field was also studied. The calculated magnetization follows from the expression:

$$\boldsymbol{M}=\frac{\boldsymbol{m}}{A_\Delta d}=\frac{1}{2A_\Delta d}\int_{A_\Delta} d^2r'\boldsymbol{r}'\times\boldsymbol{J}(\boldsymbol{r}_i,\boldsymbol{r}')$$
$$=\hat{z}\frac{1}{A_\Delta d}\int_{A_\Delta} d^2r' g(\boldsymbol{r}_i,\boldsymbol{r}'), \tag{14}$$

where $A_\Delta=\sqrt{3}a^2/4$ is the triangle area, $\boldsymbol{r}'=\boldsymbol{x}'+\boldsymbol{y}'$ is a two-dimensional vector representing a point in the triangle, $\boldsymbol{r}_i$ represents the dependence of the supercurrents on the positions of the vortex cores, and $\boldsymbol{m}$ is the magnetic dipole moment generated by $\boldsymbol{J}=\nabla\times\hat{z}g$ (cf. Sec. II). Since we are dealing with a thin superconducting triangle, $\boldsymbol{M}=M\hat{z}$. For the stable configurations, Eq. (14) was computed by using the supercurrents produced by the vortices at $\boldsymbol{r}_i$, $i=1,\ldots,N$.

In Fig. 5, we present the applied magnetic field dependence of the magnetization for the singly quantized vortex configurations, as well as for the $(1g2)$ and the $(3s1,1g2)$-states. The equilibrium magnetization is depicted by the thick line.

In our simulation, the $(3s1,1g2)$-state decays at $H_a=0.0043$ to the $(1s1,1g2)$-state. This state decays at $H_a=0.0032$ to the $(1g2)$-state. The doubly quantized vortex is expelled at $H_a=0.0005$. The $(1g2)$-state can be stable at $H_a\to 0$, although it is possible that transitions (such as, vortex

TABLE I. $H_{unst}$ and the initial $H_1$ and the final $H_2$ fields of the region over which a given vortex configuration is the ground state. The second column shows the nomenclature for each ground-state configuration (see Fig. 3). In the last column, the field range $\Delta H_{stab}=H_2-H_1$ is listed. The $L=37$ state does not present $H_2$ and $\Delta H_{stab}$ because this was the highest vorticity state we simulated.

| $L$ | Configuration | $H_{unst}$ | $H_1$ | $H_2$ | $\Delta H_{stab}$ |
|---|---|---|---|---|---|
| 0 | () | 0.0000 | 0.0000 | 0.0033 | 0.0033 |
| 1 | ($t1s1$) | 0.0000 | 0.0034 | 0.0051 | 0.0018 |
| 2 | ($t1s1+l1s1$) | 0.0024 | 0.0052 | 0.0059 | 0.0007 |
| 3 | ($t3s1$) | 0.0022 | 0.0059 | 0.0075 | 0.0016 |
| 4 | ($t4s1$) | 0.0035 | 0.0075 | 0.0085 | 0.0010 |
| 5 | ($t3s1+l2s1$) | 0.0051 | 0.0085 | 0.0091 | 0.0005 |
| 6 | ($t3s1+l3s1$) | 0.0045 | 0.0091 | 0.0107 | 0.0016 |
| 7 | ($t4s1+l3s1$) | 0.0067 | 0.0107 | 0.0115 | 0.0007 |
| 8 | ($t4s1+l4s1$) | 0.0073 | 0.0115 | 0.0124 | 0.0009 |
| 9 | ($t6s1+l3s1$) | 0.0079 | 0.0124 | 0.0129 | 0.0005 |
| 10 | ($t6s1+l4s1$) | 0.0075 | 0.0129 | 0.0146 | 0.0016 |
| 11 | ($t6s1+l5s1$) | 0.0099 | 0.0146 | 0.0153 | 0.0007 |
| 12 | ($4t3s1$) | 0.0106 | 0.0154 | 0.0161 | 0.0007 |
| 13 | ($r9s1+l4s1$) | 0.0108 | 0.0161 | 0.0170 | 0.0009 |
| 14 | ($t10s1+l4s1$) | 0.0118 | 0.0170 | 0.0174 | 0.0004 |
| 15 | ($t10s1+l5s1$) | 0.0112 | 0.0174 | 0.0191 | 0.0017 |
| 16 | ($t10s1+l6s1$) | 0.0138 | 0.0191 | 0.0199 | 0.0008 |
| 17 | ($l6s1+t6s1+l5s1$) | 0.0146 | 0.0199 | 0.0206 | 0.0007 |
| 18 | ($r13s1+l5s1$) | 0.0149 | 0.0206 | 0.0213 | 0.0007 |
| 19 | ($r14s1+l5s1$) | 0.0153 | 0.0213 | 0.0223 | 0.0010 |
| 20 | ($t15s1+l5s1$) | 0.0163 | 0.0223 | 0.0225 | 0.0002 |
| 21 | ($t15s1+l6s1$) | 0.0157 | 0.0225 | 0.0243 | 0.0018 |
| 22 | ($t15s1+l7s1$) | 0.0186 | 0.0243 | 0.0251 | 0.0008 |
| 23 | ($r16s1+l7s1$) | 0.0194 | 0.0251 | 0.0257 | 0.0006 |
| 24 | ($r18s1+l6s1$) | 0.0202 | 0.0257 | 0.0266 | 0.0008 |
| 25 | ($r19s1+l6s1$) | 0.0204 | 0.0266 | 0.0273 | 0.0007 |
| 26 | ($r20s1+l6s1$) | 0.0207 | 0.0273 | 0.0281 | 0.0008 |
| 27 | ($t21s1+l6s1$) | 0.0216 | 0.0282 | 0.0284 | 0.0002 |
| 28 | ($t21s1+l7s1$) | 0.0218 | 0.0284 | 0.0302 | 0.0018 |
| 29 | ($t21s1+l8s1$) | 0.0240 | 0.0302 | 0.0310 | 0.0008 |
| 30 | ($l8s1+t15s1+l7s1$) | 0.0248 | 0.0310 | 0.0317 | 0.0006 |
| 31 | ($l8s1+r17s1+l6s1$) | 0.0255 | 0.0317 | 0.0325 | 0.0008 |
| 32 | ($r17s1+l7s1+l8s1$) | 0.0265 | 0.0325 | 0.0330 | 0.0005 |
| 33 | ($r26s1+l7s1$) | 0.0264 | 0.0331 | 0.0340 | 0.0009 |
| 34 | ($r27s1+l7s1$) | 0.0267 | 0.0340 | 0.0348 | 0.0008 |
| 35 | ($t28s1+l7s1$) | 0.0276 | 0.0348 | 0.0349 | 0.0001 |
| 36 | ($t28s1+l8s1$) | 0.0280 | 0.0349 | 0.0370 | 0.0021 |
| 37 | ($t28s1+l9s1$) | 0.0300 | 0.0370 | | |

expulsion or splitting of the giant vortex in a multivortex state) occur at fields higher, but close, to $H_a=0$ due to thermal fluctuations.

The values of $\Delta H_{stab}$ versus the number of vortices of ground-states configurations are shown in Fig. 6. One may observe that the vortex states with the number of SQV equal to the triangular numbers $N'=n(n+1)/2$, $n=1,2,3,\ldots$, have a field range ($\Delta H_{stab}$) over which they are ground states much larger than the other configurations. Apart from the $L=0$ state, those highly stable have $\Delta H_{stab}\approx 0.0016$. Another interesting feature comes from the fact that the configurations with one less vortex than $N'$, i.e., $N=N'-1$ (except $N=2$), present a rather narrow ground-state field region ($\Delta H_{stab}\approx 0.0005$ for $L=5$, $L=9$, and $L=14$, while $\Delta H_{stab}\approx 0.0002$ for $L=20$ and $L=27$), which resembles the behavior of the electronic shells in atoms (noble gases do not in-

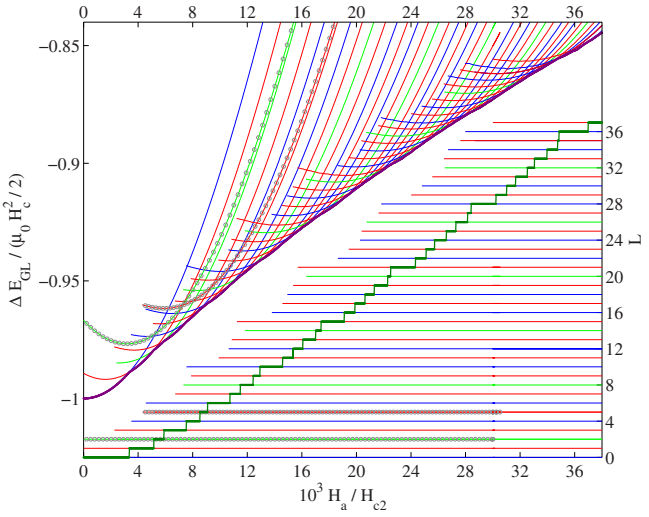


FIG. 4. (Color online) Energy (left axis) and total vorticity $L$ (right axis) dependence on the applied field $H_a$ for ground-states configurations from $L=0$ until $L=37$. Alternating colors are used to help visualization. The lines stop at a critical field $H_{unst}$, below which the given configuration ceases to be stable. The thick green and purple lines depict the region over which a given configuration with $L=N$ vortices is the ground state. The $L=2$, $N=1$ and $L=5$, $N=3$ stable configurations are also shown by lines with gray circles. Notice that the $L=2$, $N=1$ and $L=5$, $N=3$ configurations have higher energy than the corresponding $N=3$ and $N=5$ SQV configurations.

teract easily because of their closed electronic shells, while F and Cl are highly electronegative). Also, our results yield that the $L=35$ configuration is a ground state for a very narrow field range. Moreover, for $L \leq 21$, the configurations with number of vortices $N=N'-2$ appear to have quite broad

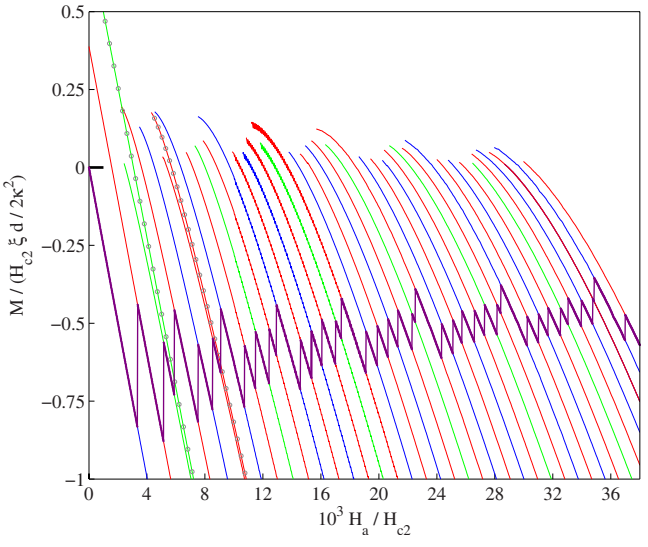


FIG. 5. (Color online) Dependence of the magnetization on the applied field $H_a$ for ground-states configurations from $L=0$ to $L=37$. Alternating colors are used to help visualization. The thick line depicts the equilibrium magnetization. The magnetization for the $L=2$, $N=1$ and $L=5$, $N=3$ stable configurations are depicted by lines with circles.

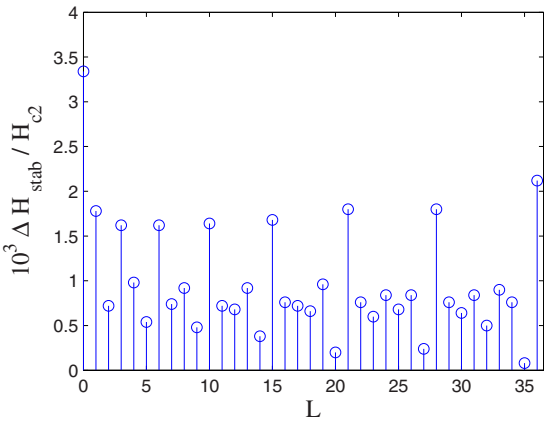


FIG. 6. (Color online) $\Delta H_{stab}$ versus the number of vortices of ground-states configurations.

field region, where they are ground states $\Delta H_{stab} \approx 0.0009$. The other configurations have $\Delta H_{stab} \approx 0.0007$. Nevertheless, for $H > 21$ the behavior of $\Delta H_{stab}$ versus the number of vortices becomes more intricate.

As it would be expected, the configurations with number of SQV equal to $N'=n(n+1)/2$, $n=1,2,3,\ldots$ also have lower $H_{unst}$ than the other configurations. This feature—together with large ground-state region—might be understood as a result of the fact that those configurations have threefold and middle-plane reflection symmetries (the symmetries of the equilateral triangle) as well as the sixfold Abrikosov lattice symmetry. In other words, those configurations are well adjusted both to the sample geometry and to the vortex-vortex interaction.

Finally, different configurations with the same number of vortices may present different magnetic field stability range, i.e., different $H_{unst}$ values.

### B. Metastable vortex configurations

#### *1. Singly quantized vortices*

For SQV, we obtained usually few distinct configurations with given $L$, $N$, and $H_a$ for a typical simulation with 1000 attempts. Low total vorticity states, ranging from $L=0$ to $L=37$, with magnetic field up to $0.05H_{c2}$, were considered. For example, our numerical procedure (with singly quantized vortices) generates only one stable configuration for $L=4,13,22,31$ at $H_a=8\times10^{-3}$, $1.7\times10^{-2}$, $2.3\times10^{-2}$, and $3.4\times10^{-2}$, respectively, but seven different stable configurations for $L=7$ at $H_a=4\times10^{-2}$. Of course, it is possible that not all stable configurations were generated, even after performing 1000 attempts. Nevertheless, this approach yields a rather satisfactory picture of the sample space of the stable configurations at a given field with a reasonable computational time.

The stable configurations for $L=9$ at $H_a=1.3\times10^{-2}$ and $L=27$ at $H_a=3.1\times10^{-2}$ are depicted in Fig. 7. The red lines appearing in Fig. 7 are used in the same way as in Fig. 3. The energy and the fraction of occurrence of each configuration are shown, as well as its symmetries (if exists). For the $L=9$, the lowest-energy configuration is the one having

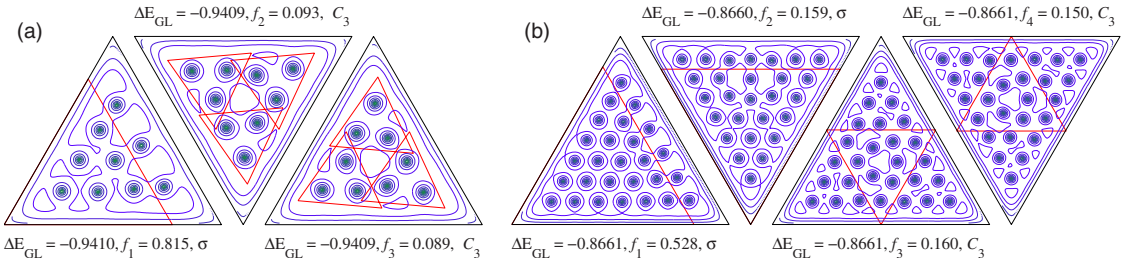


FIG. 7. (Color online) Current streamlines of the metastable vortex configurations (a) $L=9$ for $H_a=0.0130$ and (b)$L=27$ for $H_a=0.0310$. The energy ($\Delta E_{\mathrm{GL}}$) and the fraction of occurrence ($f_i$, where $i$ refers to a different configuration number) of each configuration is depicted on the top or on the bottom of each figure. $\sigma$ represents middle-plane reflection symmetry and $C_3$ represents threefold axial rotation symmetry. Notice that configurations, with threefold axial rotation symmetry, do not necessarily have lower energy than configurations with middle-plane reflection symmetry. The red straight lines are drawn to help visualization.

middle-plane reflection symmetry ($t6s1+l3s1$) [depicted in Fig. 7(a) at left]. This configuration resulted from about 82% of 1000 attempts. The ones with threefold axial rotation symmetry ($3t3s1$) [Figs. 7(a) in the middle and at right]—whose energies are slightly higher than the former—appeared each about 9% of the total number of attempts. Because these configurations lack middle-plane reflection symmetry, there can be two distinct threefold axial rotation symmetry configurations, each being the mirror reflection of the other, appearing with similar frequencies. These configurations can be labeled $(3t3s1)^d$ and $(3t3s1)^l$ in the same way as some molecules can appear as dextrogirous ( $^d$) and levogirous ( $^l$).

For $L=27$ at $H_a=3.1\times10^{-2}$, the configuration (with middle-plane reflection symmetry) having the lowest energy is the ($t21s1+l6s1$) shown at the left of Fig. 7(b), with slightly lower energy than the configurations (with threefold axial rotation symmetry) depicted in the middle and at right of Fig. 7(b). The energy difference is within our calculation accuracy; therefore, we may say that they have approximately the same energy value at that value of $H_a$. These latter two configurations differ from each other in the same manner as the configurations presented in the right of Fig. 7(a). They can be viewed as formed by a $L=9$ configuration in the center surrounded by three $L=6$ configurations. The $L=9$ configuration is one of the metastable states, which can be dextrogirous or levogirous. Therefore, those $L=27$ configuration can be labeled ($t9s1^d+3t6s1$) and ($t9s1^l+3t6s1$), where ($t9s1$) accounts for the ($3t3s1$) configuration mentioned before. Also, whereas the configuration with the lowest energy appears about 53% of all attempts, the percentage of occurrence of the other stable configurations is about 16%. The configuration ($r20s1+l7s1$) depicted in the middle left of Fig. 7(b) has higher energy than the other three configurations and appeared in about 16% of the attempts.

Regarding the configuration symmetries, the mirror plane reflection appeared more frequently than the threefold axial rotation symmetry. Also, the configurations having the former symmetry are usually the lowest-energetic ones, even in the cases where configurations having threefold rotation symmetry or both were obtained. Therefore, the presence of symmetries is not directly correlated with lower-energetic states.

The number of stable configurations can differ for different values of the magnetic field. For example, for $L=12$ one stable ($12s1$) configuration at $H_a=1.6\times10^{-2}$ (cf. Fig. 3) is obtained, while three different ones are generated at $H_a=3.6\times10^{-2}$ (see Fig. 8). The lowest-energy configuration is depicted in the left of Fig. 8. In the nomenclature developed previously, this is the ($4t3s1$) configuration. However, the captions in the middle and in the right of Fig. 8 show two other higher-energy configurations [which could be named $(r7s1+l5s1)^d$ and $(r7s1+l5s1)^l$], which do not possess any clear symmetry and which are stable only at fields above $\sim$0.0300. Other different configuration for $L=12$ is stable at $H_a\approx0.0460$. If we start with this configuration and decrease $H_a$, at some $H_{\mathrm{unst}}$ this configuration decays in one of the configurations shown in Fig. 8. If it results in the configuration depicted in Fig. 8(b), for example, and $H_a$ is further decreased, at some other $H_{\mathrm{unst}}$, the configuration decays in the lowest-energy configuration. It is also interesting to observe that at $H_a=0.0360$, the configurations with higher energy occur more frequently than the one with lowest energy with the same total vorticity. Nonetheless, configurations with higher total vorticity have a lower energy at these magnetic fields and, therefore, have much greater probability of being obtained.

### *2. Multiply quantized vortices*

We discuss now the case of MQV. One interesting possibility was that one configuration containing MQV might

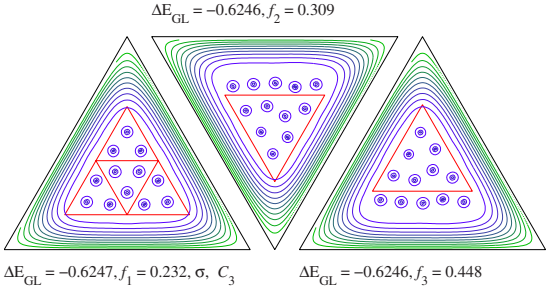


FIG. 8. (Color online) The same as Fig. 7, but for the metastable vortex configurations with $L=12$ at $H_a=0.0360$. The configuration appearing at left is the same configuration depicted in Fig. 3 but at a higher magnetic field. The green (blue) lines depict higher (lower) values of the streamline function. As in Fig. 3, red straight lines are drawn to help visualization.

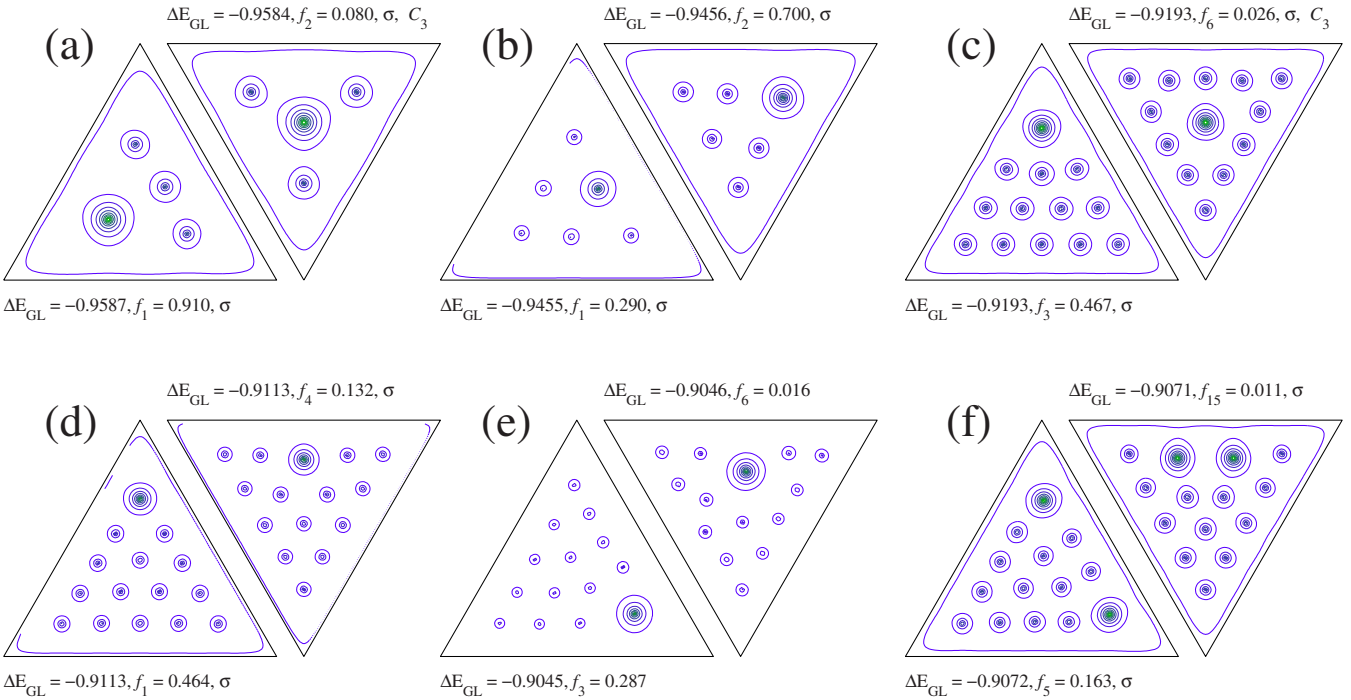


FIG. 9. (Color online) The same as Fig. 7, but for the following configurations containing multiply quantized vortices: (a) $L=5$, $(3s1,1g2)$ at $H_a=0.0080$; (b) $L=7$, $(5s1,1g2)$ at $H=0.0110$; (c) $L=14$, $(12s1,1g2)$ at $H_a=0.0170$; (d) $L=16$, $(14s1,1g2)$ at $H_a=0.0190$; (e) $L=16$, $(13s1,1g3)$ at $H_a=0.0190$; and (f) $L=16$, $(12s1,2g2)$ at $H_a=0.0190$.

have a lower energy than one containing only singly quantized vortices. One might think that this would be particularly probable when a given singly quantized vortex configuration does not satisfactorily match the geometry of the superconductor.

However, when multiply quantized are considered, the number of different configurations grows enormously with increasing total vorticity $L$. For example, for $L=5(L=7)$ with three (five) SQV and one doubly quantized vortex at $H_a=0.0110$, we obtained two different configurations, whereas for $L=16$ with 12 SQV and two doubly quantized vortices at $H_a=0.0190$, 52 different configurations were observed by performing 500 attempts. Therefore, we limited ourselves to $L\leq 18$, and performing typically 500 attempts. Our aim was neither to obtain all the possible stable configurations nor the state with lowest energy but rather to compare the obtained stable configurations containing multiply quantized vortices with those containing only SQV.

The following vortex configurations were studied: $L=5$, $(3s1,1g2)$ at $H_a=0.0080$ and at $H_a=0.0110$; $L=7$, $(5s1,1g2)$ at $H_a=0.0110$; $L=8$, $(6s1,1g2)$ and $(5s1,1g3)$ at $H_a=0.0120$; $L=9$, $(7s1,1g2)$ and $(6s1,1g3)$ at $H_a=0.0130$; $L=11$, $(9s1,1g2)$ at $H_a=0.0150$; $L=12$, $(10s1,1g2)$ and $(9s1,1g3)$ at $H_a=0.0160$; $L=13$, $(11s1,1g2)$ and $(10s1,1g3)$ at $H_a=0.0170$; $L=14$, $(12s1,1g2)$ at $H_a=0.0170$; $L=16$, $(14s1,1g2)$, $(13s1,1g3)$ and $(12s1,2g2)$ at $H_a=0.0190$; $L=17$, $(15s1,1g2)$ and $(14s1,1g3)$ at $H_a=0.0200$; $L=18$, $(16s1,1g2)$ and $(15s1,1g3)$ at $H_a=0.0210$.

Some configurations containing multiply quantized vortices are shown in Fig. 9. Not all the obtained configurations are presented for $L=14$ and $L=16$. The energy, the fraction of occurrence, and the symmetries of each configuration are shown on the top or on the bottom of each frame. Most of the configurations we observed do not have any particular symmetry. Middle-plane reflection appears more frequently than the threefold axis rotation symmetry. Moreover, it is not straightforward that the appearance of a particular symmetry implies lower energy. We observed configuration without symmetries having lower energy than ones possessing middle-plane reflection, threefold axial rotation, or both symmetries. For $L=5$ at $H_a=0.0080$, the one depicted in the left of Fig. 9(a) has lower energy ($\Delta E_{\mathrm{GL}}=-0.9587$ compared to $\Delta E_{\mathrm{GL}}=-0.9584$) and higher fraction of occurrence ($\sim 90\%$ compared to $\sim 10\%$) than the one presented in the right of Fig. 9(a).[41] However, this value of energy is higher than the energy of the configuration containing only singly quantized vortices ($\Delta E_{\mathrm{GL}}=-0.9642$). For $L=7$ at $H_a=0.0110$, the configuration with lower energy is depicted in the right of Fig. 9(b) [$\Delta E_{\mathrm{GL}}=-0.9456$ with fraction of occurrence $\sim 70\%$ compared to $\Delta E_{\mathrm{GL}}=-0.9455$ occurring $\sim 30\%$, depicted in the left of Fig. 9(b)], although the difference in energy is much smaller than in the previous example. Again, the ground state corresponds to the configuration with only SQV ($\Delta E_{\mathrm{GL}}=-0.9504$). Interestingly, both configurations with lower energy are the ones with the doubly quantized vortex positioned in the corner. It seems to contradict results obtained from Ginzburg-Landau calculations,[11] which yield giant vortex at the center of the sample. Nevertheless, we would like to draw the attention to the fact that the Ginzburg-Landau results were computed for systems of small size (usually $\leq 10\xi$) compared to the sides of the superconducting triangle $a=100\xi$ considered here. The ratio between the kinetic and the core energy counterparts is larger in the latter than in the former case. For systems with size comparable to

$\xi$, superconductivity is enhanced close to narrow channels and wedges. Therefore, SQV would be positioned preferably at these regions compared to multiply quantized ones since they would present less depreciation of the superconductivity. Moreover, for small systems, giant vortex states are usually the most stable ones at magnetic fields close to $H_{c2}$. For large systems (much larger than $\xi$), the configurations can have MQV but not as the most stable states at $H \ll H_{c2}$. Since the vortex core distance to the triangle corner is much larger than $\xi$, there is no substantial overlapping of the vortex cores; thus, the spatial modulation of the superconductivity due to the geometry or magnetic field occurs far from the vortex cores. Therefore, we attribute the lower energy of configurations with MQV closer and aligned to the triangles corner (among those with the same number of vortices and total vorticity) to the depreciation of the vortex shielding currents around its core when it approaches a corner (due to the vortex images).

In Fig. 9(c), the two configurations depicted with $L=14$ and $H_a=0.0170$ have roughly the same energy ($\Delta E_{\mathrm{GL}} = -0.9193$ within the error margin $\sim 10^{-4}$). Both of them are the lowest-energetic states found with one doubly quantized vortices (the ground state containing only SQV has $\Delta E_{\mathrm{GL}} = -0.9232$). However, the one shown in the left of Fig. 9(c) occurred $\sim 47\%$, while the other one shown [in the right of Fig. 9(c)] occurred less than 3%. Figure 9(d) shows a similar example of configurations with $L=16$ [$(14s1,1g2)$, i.e., 14 singly plus one doubly quantized vortices] at $H_a=0.0190$ with the same energy (lowest among those with one doubly quantized vortex $\Delta E_{\mathrm{GL}}=-0.9113$ but higher than the one with only SQV $\Delta E_{\mathrm{GL}}=-0.9150$). Also at $H_a=0.0190$, configurations with the same vorticity, but different number of multiply vortices, are depicted in Fig. 9(e) [$(13s1,1g3)$] and in Fig. 9(f) [$(12s1,2g2)$]. Comparatively, the $(12s1,2g2)$ configurations have lower energy ($\Delta E_{\mathrm{GL}} \approx -0.9072$) than the $(13s1,1g3)$ configurations ($\Delta E_{\mathrm{GL}} \approx -0.9046$), but both have higher energy than the $(14s1,1g2)$ configurations. This is shown in Fig. 10. The energy of the obtained vortex configurations for $L=16$, but different number of vortices, is depicted in the left, while the energy for each group of MVQ configurations in the right. The number of different configurations is 2 for the $(16s1)$ state, 5 for the $(14s1,1g2)$ state, 52 for the $(12s1,2g2)$ state, and 14 for the $(13s1,1g3)$ state. The energy spectra for configurations with different number of vortices are well separated. Except for the states, containing only singly quantized vortices, the energies of the configurations with the same number of vortices form an energy "band." The separation of the energy values within one band can be better visualized in the insets at right. For all the configurations we studied—including those with only SQV—the energy difference among configurations with same total vorticity $L$ and same number of vortices $N$ ranges from about $10^{-3}$ to less than $10^{-4}$, while for configurations with same $L$ but different number of vortices (that is, containing vortices of different vorticity) the energy difference is within the $10^{-2}-10^{-3}$ range. This indicates that for these total vorticity values, the states with MQV are not ground-state configurations. Moreover, our present study only indicates that MQV configurations are metastable configurations, with nonzero, although low, probability of being observed at the magnetic fields considered. Also, we did not study the expected lifetime of each of these MQV configurations.

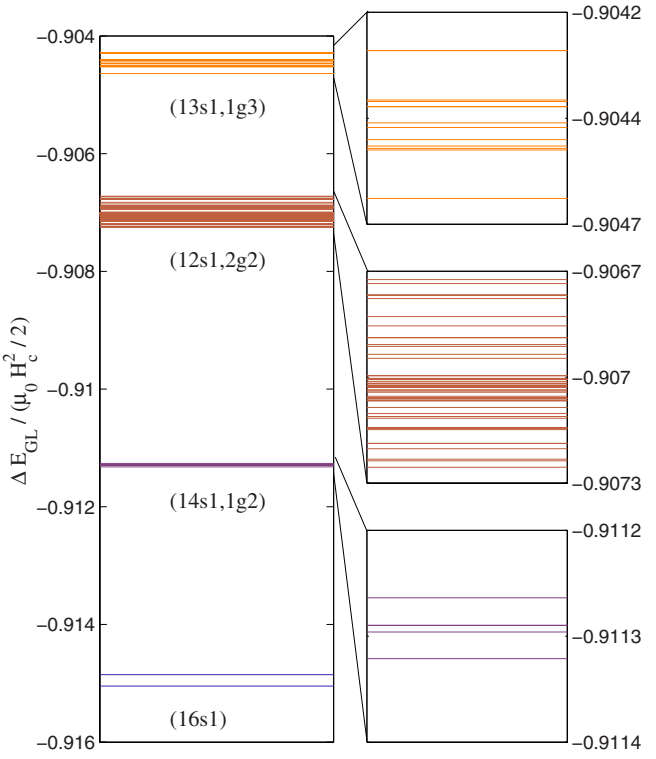


FIG. 10. (Color online) Energy of the vortex configurations for $L=16$ and $H_a=0.0190$. The $(16s1)$, $(14s1,1g2)$, $(12s1,2g2)$, and $(13s1,1g3)$ states are depicted with different colors, with a label beneath each group of lines. The insets in the right show the energy of each MQV enlarged.

The configuration depicted in the left of Fig. 9(f) has a lower energy (and occurs more frequently) than the one presented in the right of Fig. 9(f). In the former, both of the two doubly quantized vortices are placed in one of the triangle corners, while in the latter they are together along and in the middle of the triangle side. Our explanation for the lower energy of the former configuration comes from the fact that $|\Psi|^2$ is more depreciated when the two doubly quantized vortices are nearest neighbors than when they are separated. Moreover, positioning one MQV close to the sample sides or in the corner depreciates the shielding currents generated by itself (due to vortex images currents, which appear to fulfill the condition of zero net current across the boundary).

One feature we observed is that the addition of multiply quantized vortices increases the number of different configurations obtained from random initial conditions. Adding one MQV made the number of different configurations, which is typically one to seven for SQV, jump to an average of ten to 15 different configurations [minimum of two for $L=5$, $(3s1,1g2)$ and $L=7$, and maximum of 22 for $L=18$, $(16s1,1g2)$]. When another multiply quantized vortex is included, we obtained 52 different configurations. The reason for the proliferation of different configurations when considering multiply and SQV together seems to be related to the number of different arrangements of balls of different sizes inside a confined geometry. Uniformly sized balls tend to

have a lower number of different possible configurations than arrangements of balls of different sizes. It can be hinted by a given arrangement of balls of the same size: any permutation of two balls generate the same arrangement. Meanwhile, if one ball has different size from the rest, not all the permutation of two balls generates the initial arrangement. It is also known that impurities, e.g., atom 'B, in a lattice of atoms 'A, create several lattice defects, such as dislocations, vacancies, domain walls, etc., therefore, increasing the number of possible different arrangements among the atoms.

Another interesting point to be mentioned is that the configuration shown in the right of Fig. 9(e) has a lower energy than the one depicted in the left, although appeared much less frequently than the latter. For configurations with only SQV ($L=20$, 27, 30, 32, 34, and 35), we also obtained two or more configurations with roughly the same energy (energy difference smaller than $10^{-4}$) but with very different occurrence fractions. For example, for $L=30$ at $H_a=0.033$, two configurations with $\Delta E_{\mathrm{GL}}=-0.8602$ appeared in 23% and 56% of the attempts. Therefore, one may notice that configurations with the same or lower energy do not necessarily occur more frequently. This can be understood from the simple picture of two potential wells, one being narrow and deep and the other one shallow but large. Although the first has lower energy, the latter will probably be achieved more frequently, starting from a randomly chosen initial state.

## V. CONCLUSIONS

We performed a systematic study of vortex configurations in thin superconducting equilateral triangles submitted to a homogeneous external magnetic field. We calculated analytically the vortex interactions within the London approach. The vortex stable positions were obtained by a numerical procedure, which allowed us to collect different metastable states at a given magnetic field. The large number of attempts yielded a high probability of finding the states with the lowest energy. The energy of the stable configurations was computed by solving approximately the first Ginzburg-Landau equation with the phase of the order parameter calculated analytically within the London limit.

The configurations have vortices aligned to the sides or sit close to the triangles corners. Threefold axial rotation symmetry or middle-plane reflection symmetry (or both) is observed in many metastable configurations, with a tendency of the middle-plane reflection symmetry to appear more frequently. The existence of a particular symmetry does not necessarily implicate in states having lower energy. Nevertheless, configurations with middle-plane reflection symmetry occur more frequently as the ones with the lowest energy.

We obtained the ground states as function of the magnetic field. The range of stability of the vortex configurations resembles the stability of atoms in the periodic table. The states containing number of vortices equal to $N'=n(n+1)/2$, for $n$ integer, were the most stable ones for larger magnetic field ranges. This is due to the threefold axial rotation, middle-plane reflection, and Abrikosov's hexagonal lattice symmetries presented by these configurations. On the opposite side, configurations with number of vortices equal to $N=N'-1$ have the smallest magnetic field stability range. These features are closely related to the stability of noble gases (with completely filled electronic shells) as well as to the high electronegativity of elements, such as F and Cl, which need one electron to fill their electronic shells. Interestingly, configurations with $N=N'-2$ vortices have a moderately large field stability range.

Metastable states with only SQV were studied. For most configurations with given total vorticity and magnetic field, those having lower energy occurred more frequently. However, configurations with higher energy appearing more frequently than ones with lower energy were observed. This merely reflects the fact that there can be both shallow but large and narrow but deep minima in the potential landscape. Also, for fixed $L$ different configurations cease to be stable at different magnetic fields. This indicates that at higher magnetic fields, the number of different configuration might increase, although, for these values of $H_a$, configurations with higher total vorticity have lower energy, which eventually prevents the observation of the former configurations.

Finally, we investigated configurations containing both singly and multiply quantized vortices. The number of different configurations after hundreds of attempts increases enormously in the latter case. Also, for the configurations we obtained, the ones with multiply quantized vortices always had higher energy than the ones for the same $L$ and $H_a$ but with only quantized vortices. This suggests that in homogeneous superconducting samples (with size much larger than $\xi$), the coexistence of singly and multiply quantized vortices, although possible, has low probability to occur in comparison with configurations with singly quantized vortices only.

## ACKNOWLEDGMENTS

This work was supported by the Brazilian Science Agencies FACEPE under Grant No. APQ.0589-1.05/08, CNPq, and CAPES. We would like to thank C. C. de Souza Silva for helpful discussions.

*lrecabral@df.ufpe.br

[1] A. I. Buzdin and J. P. Brison, Phys. Lett. A **196**, 267 (1994).
[2] V. A. Schweigert and F. M. Peeters, Phys. Rev. B **57**, 13817 (1998).
[3] B. J. Baelus, L. R. E. Cabral, and F. M. Peeters, Phys. Rev. B **69**, 064506 (2004).
[4] L. R. E. Cabral, B. J. Baelus, and F. M. Peeters, Phys. Rev. B **70**, 144523 (2004).
[5] I. V. Grigorieva, W. Escoffier, J. Richardson, L. Y. Vinnikov, S. Dubonos, and V. Oboznov, Phys. Rev. Lett. **96**, 077005 (2006).
[6] P. A. Venegas and E. Sardella, Phys. Rev. B **58**, 5789 (1998).
[7] G. J. Stejic, A. Gurevich, E. Kadyrov, D. Christen, R. Joynt, and

D. C. Larbalestier, Phys. Rev. B **49**, 1274 (1994).
[8] G. Carneiro, Phys. Rev. B **57**, 6077 (1998).
[9] C. C. de Souza Silva, L. R. E. Cabral, and J. A. Aguiar, Phys. Rev. B **63**, 134526 (2001).
[10] A. S. Mel'nikov, I. M. Nefedov, D. A. Ryzhov, I. A. Shereshevskii, V. M. Vinokur, and P. P. Vysheslavtsev, Phys. Rev. B **65**, 140503(R) (2002).
[11] B. J. Baelus and F. M. Peeters, Phys. Rev. B **65**, 104515 (2002).
[12] B. J. Baelus, A. Kanda, N. Shimizu, K. Tadano, Y. Ootuka, K. Kadowaki, and F. M. Peeters, Phys. Rev. B **73**, 024514 (2006).
[13] E. Sardella, M. M. Doria, and P. R. S. Netto, Phys. Rev. B **60**, 13158 (1999).
[14] C. C. de Souza Silva, L. R. E. Cabral, and J. Albino Aguiar, Physica C **404**, 11 (2004).
[15] C. Meyers and M. Daumens, Phys. Rev. B **62**, 9762 (2000).
[16] S. W. S. Apolinario, B. Partoens, and F. M. Peeters, Phys. Rev. E **74**, 031107 (2006).
[17] L. F. Chibotaru, A. Ceulemans, V. Bruyndoncx, and V. V. Moshchalkov, Phys. Rev. Lett. **86**, 1323 (2001).
[18] A. A. Abrikosov, Sov. Phys. JETP **5**, 1174 (1957); Phys. Chem. Solids **2**, 199 (1957).
[19] E. H. Brandt, Rep. Prog. Phys. **58**, 1465 (1995).
[20] G. Blatter, M. V. Feigel'man, V. B. Geshkenbein, A. I. Larkin, and V. M. Vinokur, Rev. Mod. Phys. **66**, 1125 (1994).
[21] P. G. de Gennes, *Superconductivity in Metals and Alloys* (Addison-Wesley, Reading, MA, 1989).
[22] L. F. Chibotaru, A. Ceulemans, V. Bruyndoncx, and V. Moshchalkov, Nature (London) **408**, 833 (2000).
[23] V. R. Misko, V. M. Fomin, J. T. Devreese, and V. V. Moshchalkov, Phys. Rev. Lett. **90**, 147003 (2003).
[24] H. J. Zhao, V. R. Misko, F. M. Peeters, S. Dubonos, V. Oboznov, and I. V. Grigorieva, EPL **83**, 17008 (2008).
[25] J. R. Clem, J. Low Temp. Phys. **18**, 427 (1975).
[26] E. H. Brandt, Phys. Rev. Lett. **74**, 3025 (1995).
[27] A. L. Fetter, Phys. Rev. B **22**, 1200 (1980).
[28] G. R. Berdiyorov, L. R. E. Cabral, and F. M. Peeters, J. Math. Phys. **46**, 095105 (2005).
[29] L. Prigozhin, J. Comput. Phys. **144**, 180 (1998).
[30] V. G. Kogan, J. R. Clem, and R. G. Mints, Phys. Rev. B **69**, 064516 (2004).
[31] L. F. Chibotaru, A. Ceulemans, M. Morelle, G. Teniers, C. Carballeira, and V. V. Moshchalkov, J. Math. Phys. **46**, 095108 (2005).
[32] L. R. E. Cabral and J. Albino Aguiar, Physica C **468**, 722 (2008).
[33] However, this vector potential differs from the gauge obtained in Ref. 31 for triangles, which is not divergent free. The reason for this discrepancy seems to arise from the fact that in the latter, the procedure to obtain the gauge for the vector potential consisted in a series expansion, which was cut off in the first term. In fact, this result was used in one of our previous publications (Ref. 32), which yielded vortex configurations inconsistent with the known experimental data.
[34] J. Bardeen and M. J. Stephen, Phys. Rev. **140**, A1197 (1965).
[35] D. Reefman and H. B. Brom, Physica C **183**, 212 (1991).
[36] N. Grønbech-Jensen, Comput. Phys. Commun. **119**, 115 (1999).
[37] In Ref. 24, the long-range vortex interaction with its images is truncated at $\sim 6\lambda$ since it decays with $\exp(-r/\lambda)$.
[38] J. J. Barba, L. R. E. Cabral, and J. Albino Aguiar, Braz. J. Phys. **36**, 1029 (2006).
[39] However, we should point out that some values of $L$ yielded more than one configuration with the same energy within our calculation accuracy. The ones shown in Sec. IV A have the lower energy regardless this uncertainty.
[40] We refer to the coexisting singly quantized and giant vortex states by the following nomenclature $(Ps1, QgG_1, RgG_2, \ldots)$, where $P, Q, R, \ldots$, are the number of $s1$ (singly quantized) vortices, $G_1$ quantized giant vortices, $G_2$ quantized giant vortices, and so on. Therefore, $(3s1, 1g2)$ means the state containing 3 singly quantized vortices and 1 doubly (giant) quantized vortex.
[41] One may notice that although two different vortex configurations were obtained for $L=5$, $(3s1, 1g2)$ at $H_a=0.0080$ and $L=7$, $(5s1, 1g2)$ at $H_a=0.0110$, in Figs. 9(a) and 9(b) the sum of the occurrence frequencies $f$ is not equal to one. The reason for this discrepancy comes from the fact that our numerical procedures yielded configurations with $L \neq 5$ at $H_a=0.0080$ and $L \neq 7$ at $H_a=0.0110$, respectively. When the occurrence frequencies of these configurations are computed, the sum of the occurrence frequencies of each different configuration becomes equal to one.